Cement and Concrete Research 41 (2011) 64–76

Contents lists available at ScienceDirect

Cement and Concrete Research

journal homepage: http://ees.elsevier.com/CEMCON/default.asp

An integrated approach for modelling the tensile behaviour of steel fibre reinforced self-compacting concrete

V.M.C.F. Cunha [a,c], J.A.O. Barros [b,c,*], J.M. Sena-Cruz [b,c]

[a] ISISE, Engineering Department, Science and Technology School, UTAD University of Trás-os-Montes e Alto Douro, Vila Real, Portugal
[b] Structural Division, Dep. of Civil Engineering, University of Minho, Guimarães, Portugal
[c] ISISE, Institute for Sustainability and Innovation in Structural Engineering

ARTICLE INFO

Article history:
Received 27 May 2010
Accepted 17 September 2010

Keywords:
Steel fibre reinforced self-compacting concrete
Micromechanics (C)
Tensile properties (C)
Finite element analysis (C)

ABSTRACT

The present work resumes the experimental and numerical research carried out for the development of a numerical tool able of simulating the tensile behaviour of steel fibre reinforced self-compacting concrete (SFRSCC). SFRSCC is assumed as a two phase material, where the nonlinear material behaviour of SCC matrix is modelled by a 3D smeared crack model, and steel fibres are assumed as embedded short cables distributed within the SCC matrix according to a Monte Carlo method. The internal forces in the steel fibres are obtained from the stress–slip laws derived from the executed fibre pullout tests. The performance of this numerical strategy was appraised by simulating the tensile tests carried out. The numerical simulations showed a good agreement with the experimental results.

1. Introduction

In steel fibre reinforced concrete, SFRC, steel fibres and matrix are bonded together through a weak interface, which behaviour is important to understand and accurately model the mechanical behaviour of SFRC, since the properties of this composite are greatly influenced by the interface zone between fibre/matrix and, consequently, by the micro-mechanical fibre reinforcement mechanisms that are mobilized. When these composites are reinforced with low fibre volume ratios, the fibre contribution benefits arise, mainly, not to say almost exclusively, after the crack initiation.

The post-cracking behaviour of random discontinuous fibre reinforced composites can be predicted by the use of a stress–crack opening displacement relationship, $\sigma-w$. Several authors developed micro-mechanical models to obtain the $\sigma-w$ relationship, since for quasi-brittle materials, the stress–crack opening relationship that simulates the stress transfer between the faces of the crack has a significant impact on the behaviour of a structure after its cracking initiation. In the case of FRC, the $\sigma-w$ relationship can be approximated by averaging the contributions of the individual fibres bridging the matrix crack plane, defining for this purpose the probability–density functions of the centroidal distance of fibres from the matrix crack plane, and of the orientation angle [1–3]. These models, which are based on an averaging process of all the forces that are carried out by the fibres over a crack plane, can provide the general material composite behaviour with reasonable accuracy by modelling the main mechanisms of a single fibre pullout. However, in general, they do not account for some aspects, such as, fibre bending rupture and matrix spalling at the exit points of inclined fibres.

Another difficulty on the prediction of the post-cracking behaviour of a FRC in a real structure is that the material behaviour in a test specimen may differ from the behaviour of a real structural element. It is well described in literature that various casting procedures and structural shapes may result in predominant fibre orientation into parallel planes [4,5]. In the case of steel fibre reinforced self-compacting concrete, SFRSCC, the predominant fibre orientation can be along the flow itself (in the fresh state) and along the boundary surfaces due to the wall-effect [6,7]. A predefined orientation of the steel fibres parallel to the tensile direction in a test specimen may result in overestimating the post-cracking mechanical properties of the steel fibre reinforced concrete, when compared with specimens with equal amount of fibres, however with a random fibre orientation.

Having in mind the aforementioned aspects and factors that influence and contribute to the post-cracking behaviour of a FRC, approaching the FRC as a continuum material may lead to a rough estimation of the mechanical behaviour of a certain FRC structural element. Even though, material behaviour laws for FRC can be obtained with great accuracy by inverse analysis procedures of test specimens, these laws may not translate the accurate material behaviour within a specific structural element [8]. It is feasible to assume FRC as a two phase material, namely, an unreinforced concrete matrix phase and a fibre phase, with the latter one comprising information about fibre density and orientation depending on where and how the material is applied. Hence, this approach

* Corresponding author. Structural Division, Dep. of Civil Engineering, University of Minho, Guimarães, Portugal. Tel.: +351 253 510 210; fax: +351 253 510 217.
E-mail address: barros@civil.uminho.pt (J.A.O. Barros).

0008-8846/$ – see front matter © 2010 Elsevier Ltd. All rights reserved.
doi:10.1016/j.cemconres.2010.09.007

can somehow enhance the numerical simulation of FRC structures, thus excluding the use of biased material behaviour laws, i.e. from a macro-mechanical behaviour point of view, obtained from the inverse analysis of experimental tests.

Therefore, based on the prior reasoning, the present work is presented with a numerical approach where SFRC is treated as a heterogeneous medium comprised of one homogeneous phase (aggregates and paste), and another one composed of the steel fibres. The fracture process of the cementitious matrix (unreinforced) is modelled with a 3D multi-directional fixed smeared crack model. This unreinforced concrete phase is discretized by solid finite elements. On the other hand, the stress transfer between crack planes due to the fibres bridging active cracks is modelled with 3D truss elements. A nonlinear behaviour law is assigned to these last elements in order to account the fibre/matrix interface properties. These laws are based upon the micro-mechanical behaviour of the fibres. The random fibre distribution, over the matrix, is simulated with an algorithm based on the Monte Carlo method, providing a realistic distribution of the fibres over a bulk element. The developed algorithm enables to take into account factors that influence the fibre structure, such as: the so-called wall-effect and the high flowability of the SFRSCC [8]. The geometry, positioning and orientation of the fibres are subsequently inserted in a three-dimensional finite element mesh. The cable elements representing the fibres are considered as embedded elements. Within a first stage of the research, as a simplification, the embedded element is modelled with a perfectly bonded formulation. Hence, the bond–slip behaviour is simulated in an indirect fashion from the transformation of a load–slip relationship to a tensile stress–strain relation. Moreover, to the author's knowledge this kind of approach is quite novel, and within numerical models for the FRC with the same philosophy only meso-level models using lattice structures are known, e.g. [9–11].

2. Materials

The materials used in the composition of the SFRSCC, were: cement (C) CEM I 42.5R, limestone filler (LF), superplasticizer (SP) of third generation based on polycarboxilates (Glenium® 77SCC), water (W), three types of aggregates (fine river sand, FS, coarse river sand, CS, and crushed granite 5–12 mm, CA) and DRAMIX® RC-80/60-BN hooked end steel fibres (length, l_f, of 60 mm, diameter, d_f, of 0.75 mm, aspect ratio, l_f/d_f, of 80, and yield stress of 1100 MPa). The method used to define the SFRSCC composition, the mixing procedure and other properties of the SFRSCC in the fresh state can be found elsewhere [12].

To study the SFRSCC tensile post-cracking behaviour, two batches with distinct fibre contents (C_f), 30 and 45 kg/m^3 were used. Table 1 includes the compositions that have best fitted self-compacting requirements for the adopted two fibre contents. Remark that in Table 1, WS is the water necessary to saturate the aggregates, and W/C is the water/cement ratio. The WS parcel was not used to compute the W/C ratio. The fibre pullout tests were performed on the SCC medium with a fibre content of 30 kg/m^3.

For determining the SFRSCC properties in the fresh state, the Abrams cone was used in inverted position (concrete flowed through the small orifice of the cone). A total spread over 700 mm was measured and no sign of segregation was detected as the mixture showed good homogeneity and cohesion.

3. Experimental research

3.1. Fibre pullout tests

3.1.1. Series of tests, preparation of specimens and SCC properties

The pullout tests were divided into two main groups, according to the geometry type of used fibres: hooked ends and smooth. The influence of the fibre's embedded length, L_b, (10, 20 and 30 mm) and fibre's orientation (0, 30 and 60°) on the pullout response was assessed in both groups. Each series of the smooth fibres comprises three specimens, whereas six specimens compose each series of the hooked fibres. Smooth fibres were obtained by cutting the hooked ends of the RC-80/60-BN fibres with pliers. Code names were given to the test series, which consist on alphanumeric characters separated by underscores. The first character indicates the fibre type (S — smooth; H — hooked), the second string indicates the embedded length in mm (for instance, L_b10 represents a fibre embedded length of 10 mm) and finally the last numeral indicates the angle between the fibre and the fibre pullout load direction, in degrees. Due to technical problems, the series S_L_b10_0 and S_L_b10_30 could not be correctly tested, therefore they are not presented.

The pullout tests on single steel fibres were performed using cored SCC specimens. A special mould was designed, able to accommodate 81 fibres fixed at its bottom (more details can be found elsewhere, [8]). This device was used to cast the 81 pullout specimens simultaneously, allowing a correct placement of the fibre and keeping the desired L_b and inclination angle for the fibre. After casting, the SCC slab was cured at a temperature of 20 °C and a relative humidity of about 95%. After 30 days, the SCC slab was demolded, and cylindrical cores containing, each one, a single fibre was drilled from the slab. The diameter and height of each specimen was 80 mm.

The fibre pullout tests were performed at approximately 180 days after concrete casting. The concrete compressive strength was assessed by testing three cubic specimens with an edge length of 150 mm. The average value of the concrete compressive strength, at the age of the fibre pullout tests, was 83.4 MPa with a coefficient of variation of 0.9%. This strength in cubes corresponds to an equivalent average strength in cylinders of 69.5 MPa, if adopting an approximate ratio between the strength in cubes and cylinders of 1.2 [13,14].

3.1.2. Test setup

The specimen is mounted in a steel supporting system, see Fig. 1. This frame incorporates a steel system composed by a plate connected to a cylinder that is fixed to the testing machine frame. The cylinder/machine connection allows free rotations of the entire steel frame. A steel ring is coupled to the aforementioned steel system by three steel screws. The protruding end of the steel fibre is fastened to a standard grip that allows a secure hold of the fibre.

For the measurement of the fibre pullout slip, three LVDT's (linear stroke ±5 mm) were used. In order to exclude measuring deformations of the testing rig and fibre slip at the grip, the LVDT's were fixed at the upper steel ring and touching the bottom surface of an aluminium plate fastened to the fibre. The plate was fixed to the fibre

Table 1
Compositions for 1 m^3 of SFRSCC.

Cement type I 42.5R (C) [kg]	Limestone filler (LF) [kg]	Water (W) [dm^3]	Water to saturate aggregates (WS) [dm^3]	Super plasticizer (SP) [dm^3]	Fine sand (FS) [kg]	Coarse sand (CS) [kg]	Crushed calcareous (CA) [kg]	Steel fibres (Cf) [kg]	W/C
359.4	312.2	96.9	64.7	6.9	108.2	709.4	665.2	30	0.29
401.7	344.2	117.3	65.4	7.6	178.3	668.1	668.1	45	0.31

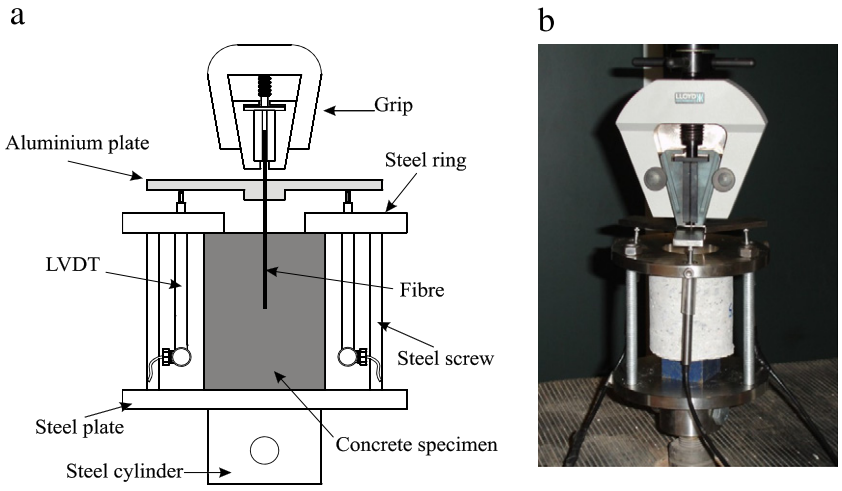

Fig. 1. Setup of the single fibre pullout test. (a) schematic representation; b) photo.

with two fine screws and was used as a support for this LVDT configuration (Fig. 1). The deformation of the steel frame in which the LVDT's were fixed is marginal, due to its considerable stiffness. Since the three LVDT's were disposed around the test specimen forming an angle of 120° between consecutive LVDT's, the actual slip of the fibre is the average of the three LVDT's readouts. The closed-loop displacement control was performed by the testing machine internal displacement transducer, at a rate of 10 μm/s.

3.1.3. Results

3.1.3.1. Failure modes. The totality of both hooked and smooth aligned fibres were completely pulled out. In the case of hooked fibres, after debonding of the fibre/matrix interface, the hooked was fully smoothened. This failure mode was designated as FM1. A similar failure mode, FM2, was observed for some inclined fibres, however, in opposite to aligned fibres, spalling of the matrix at the fibre bending point was observed. Nevertheless, the most common failure mode observed during the pullout tests of inclined hooked fibres was fibre rupture, FM3. Another observed failure mode, FM4, was by matrix spalling. In this case, the fibre was almost fully pulled out from the concrete specimen. However, when the embedded end of the fibre approaches the exit point of the concrete matrix, a portion of concrete near the fibre bending point was detached. This failure mode was only observed for a few fibres with an inclination angle of 60° and a $L_b = 10$ mm. Premature fibre or matrix failures were observed, exclusively in pullout specimens with inclined fibres. Moreover, fibre rupture was the predominant failure mode for a 30° inclination angle, whereas for an angle of 60° and lower embedded lengths matrix failure was also registered. For hooked inclined fibres, the fibre rupture occurred for stresses lower than the fibre's tensile strength. This can be explained by the fact that inclined fibres are submitted to a mixed tensile–bending mode. Hence, as the inclination angle increases, the bending moment will increase resulting in a decrease of the fibre's tensile rupture stress. The failure modes observed for each series are indicated in Table 2. When more than one failure mode occurred for a specific series, the number of specimens corresponding to each failure type is indicated between parentheses.

3.1.3.2. Pullout load–slip curves. The average pullout load–slip curves for the tested series are depicted in Fig. 2. In general, for both analyzed hooked and smooth aligned fibres, the configuration of the pullout load–slip curve was similar, regardless the fibre embedded length but, as expected, the peak load and the dissipated energy increased with L_b (see Fig. 2a). In smooth fibres, after the peak load was attained a sudden drop was observed, which corresponds to an abrupt increase of damage at the fibre/paste interface (unstable debond). Afterwards, fibre/paste friction was the commanding mechanism of the pullout behaviour. In this part of the post-peak branch, the load decreased with the increase of slip, since the available frictional area decreases, as well as the roughness of the failure surface. On the other hand, the post-peak load decay in hooked fibres was not so abrupt than in smooth fibres, since with the increase of the slip the fibre mechanical anchorage started to become progressively mobilized. At an approximately 4.5 mm slip (corresponding approximately to the smoothened hook length), the pullout process occurs under frictional resistance in similitude to smooth fibres.

In the case of hooked fibres with a 30° inclination angle, as previously seen, two failure modes occurred, which were reflected into two distinct types of pullout–slip curves. In Fig. 2b, the average curve is represented up to the slip where the fibre rupture took place; therefore the curve averaging was performed only up to a slip correspondent to the peak load. For some specimens, sudden load drops were observed before attaining the peak load. This was a consequence of matrix wedges that have spalled. After each

Table 2
Overview of the experimental pullout results.

Series	Failure mode	N_{max} [N]	CoV [%]	s_{peak} [mm]	CoV [%]
S_L_b10_60	*FM4*	154.2	43.8	3.34	45.6
S_L_b20_0	*FM1*	77.4	2.0	0.12	11.8
S_L_b20_30	*FM2*	173.5	18.2	0.19	7.4
S_L_b20_60	*FM2*	172.8	8.7	2.02	2.0
S_L_b30_0	*FM1*	155.2	9.7	0.25	14.4
S_L_b30_30	*FM2*	203.7	13.8	0.38	32.3
S_L_b30_60	*FM2*	189.4	15.0	2.17	11.8
H_L_b10_0	*FM1*	321.8	5.6	0.59	8.7
H_L_b10_30	*FM2*(2)*, *FM3*(4)	360.9	13.9	0.94	11.4
H_L_b10_60	*FM3*(5), *FM4*(1)	342.0	2.3	2.40	20.8
H _L_b20_0	*FM1*	347.8	2.8	0.65	9.4
H _L_b20_30	*FM2*(2), *FM3*(4)	400.1	4.9	1.00	9.7
H _L_b20_60	*FM3*	335.2	3.0	2.33	15.1
H _L_b30_0	*FM1*	388.2	1.6	0.69	11.0
H _L_b30_30	*FM3*	416.0	3.4	0.80	19.3
H_L_b30_60	*FM3*	365.1	2.5	2.64	23.2

FM1 — fibre pullout; *FM2* — fibre pullout with matrix spalling; *FM3* — fibre rupture; *FM4* — matrix spalling.
*(i) — *i* is the number of specimens with this type of failure mode.

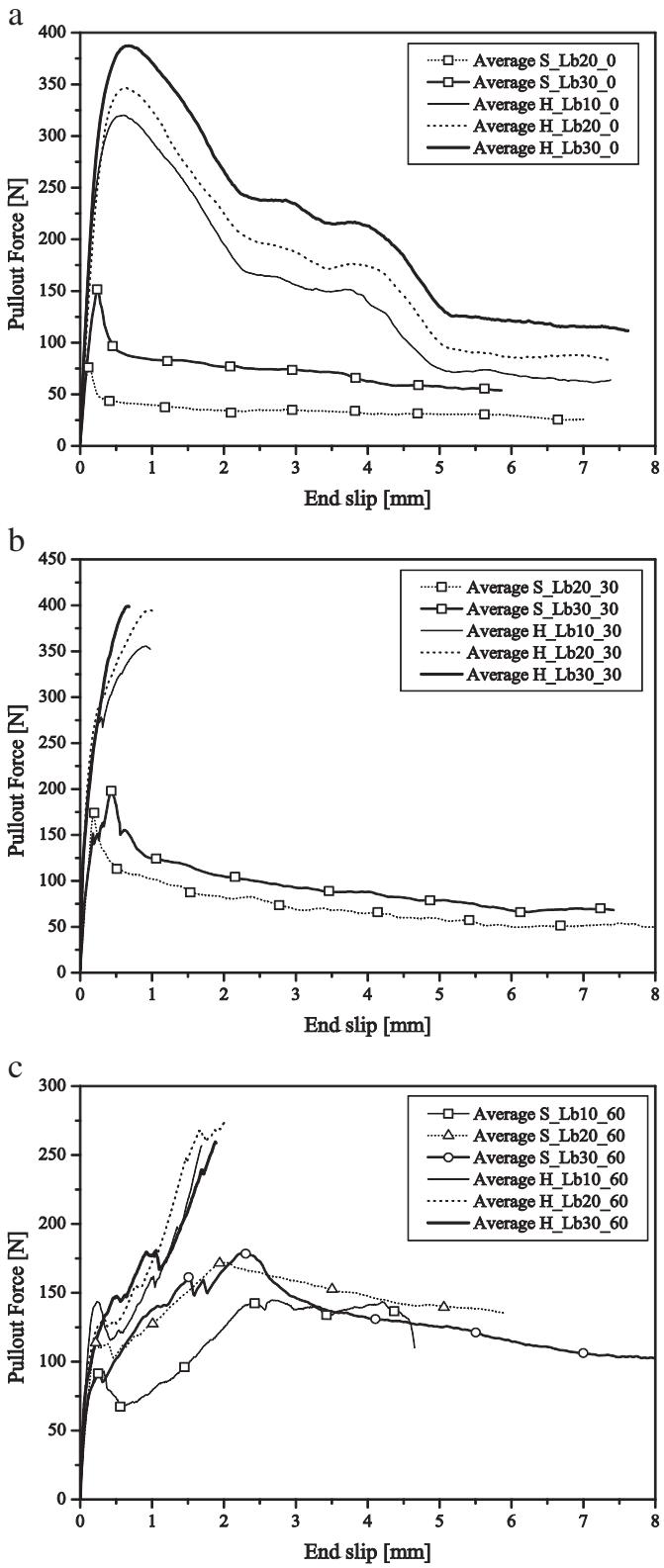

Fig. 2. Average pullout load–slip curves for a fibre inclination angle: (a) 0°, (b) 30° and (c) 60°.

completion of wedge spalling off, a new more stable wedge was formed, and the remaining fibre segment embedded in the matrix was then pulled out. On the other hand, for the post-peak behaviour of smooth fibres with an inclination angle of 30° the load also decreases with the increase of slip. Comparatively to the aligned smooth fibres, the load decay is lesser abrupt, since the influence of the frictional resistance is more significant for inclined fibres.

A completely distinct behaviour was observed for the series with an inclination angle of 60° (Fig. 2c). As previously seen, the hooked series with the latter inclination angle failed by fibre rupture, with the exception of one specimen [8], whereas in the series of smooth fibres were fully pulled out. As the inclination angle increased, the stresses concentration at the fibre exit point from the matrix increased, therefore the concrete matrix is more prone to cracking and spalling. In terms of pre-peak behaviour, this was reflected in a significant loss of stiffness. Comparing Fig. 2b, and Fig. 2c, it can be perceived that for the series with a 60° angle, cracking and spalling started for a lower load level. Moreover, as a larger portion of concrete was pushed or pulled out, a larger fibre length can be more easily bent. Therefore an additional displacement correspondent to the free deformation of the fibre's protruding part will be added to the measured slip, which promotes the stiffness decrease up to the peak load. Regarding the post-peak in smooth fibres, smoother load decay was observed than in case of smooth fibres aligned at 30° angle, since for a 60° inclination angle the frictional resistance due to the force component perpendicular to the fibre axis is much higher.

3.1.3.3. Effect of the fibre embedded length. In Table 2 are indicated both the average values of the peak pullout load, N_{max}, and the corresponding coefficient of variation, CoV. Generally, the N_{max} increased linearly with the L_b for both hooked and smooth fibres. The series H_L_b_60 was the only exception, since it was observed a decrease on the N_{max} when L_b increased from 20 mm to 30 mm. In the case of aligned fibres the influence of L_b was more significant on the smooth fibres, since an increase of more than 100% on N_{max} occurred, increasing L_b from 20 to 30 mm, while smaller increments were registered in the hooked fibres. In fact, for hooked fibres the increment of L_b from 10 to 30 mm provided an increase on the N_{max} of about 20%. These results demonstrate that the pullout response of hooked fibres at given L_b is predominantly influenced by the mobilization and smoothening of the hook, which is in accordance with published findings [15,16]. For inclined smooth fibres, in resemblance to the aligned hooked fibres, the increase of N_{max} with the increase of L_b was also relatively small, respectively, 17% and 23% for an inclination angle of 30° and 60° (for the comparison between $L_b = 20$ mm and $L_b = 30$ mm). These results point out that, in inclined fibres, the enhanced frictional resistance due to the force component normal to the fibre axis (due to the fibre inclination) plays a more important role on the peak pullout load than the L_b. This is even more relevant on the inclined hooked fibres, since both mechanical deformation of the hook and frictional resistance actuate together. Therefore, for the latter series, the increase of N_{max} with L_b will be smaller than for smooth fibres. Moreover, this increment decreases with the inclination angle (20%, 15% and 7%, respectively for the hooked series with a 0°, 30° and 60° — these values correspond for the comparison between $L_b = 10$ mm and $L_b = 30$ mm).

The average values of the slip at peak pullout load, s_{peak}, and the corresponding coefficient of variation, CoV, are indicated in Table 2. For both smooth and hooked aligned fibres a slight increase of s_{peak} with L_b was observed, whereas for inclined fibres no clear tendency of the influence of the L_b on the s_{peak} was found. The high values obtained for the CoV hampers the perception of a clear trend between L_b and s_{peak} for the inclined fibres' series.

A detailed overview of the pullout toughness of the current experimental tests can be found elsewhere [8]. Nevertheless, the main conclusion that can be drawn is that, the overall toughness is markedly influenced by the type of failure mode, since fibre fracture significantly reduces the toughness when compared to the cases where fibres underwent a complete pullout.

3.1.3.4. Effect of the fibre inclination angle. In general, the N_{max} increases up to an inclination angle of 30° and then decreases for 60° angle. For both hooked and smooth fibres the highest maximum pullout load was observed for an inclination angle of 30°. However, the increase of the maximum pullout load with the inclination angle was more significant on the smooth fibre series. The series of smooth fibres with a 30° inclination angle had a N_{max} 30% and 125% higher than the aligned smooth fibre series, respectively, for $L_b = 30$ mm and $L_b = 20$ mm. On the other hand, for the hooked fibre series with a 30° inclination angle, the N_{max} is just 7% to 15% higher than aligned hooked fibre series. In spite of the increase of the frictional pullout component with the inclination angle, increasing the angle from 30° to 60° led to a slight decrease on the N_{max}. Remember that for the series of inclined hooked fibres, fibre rupture was the commanding failure mode. Moreover, the average peak pullout load was smaller for the series with a 60° inclination angle than for 30°.

The slip at peak load, s_{peak}, increased with the inclination angle for both hooked and smooth fibres, especially in the smooth fibres. From 0° to 30° a slight increase on s_{peak} was observed, while a significant increase of speak was registered from 30° to 60°. In fact, for the series of smooth fibres with 60° inclination angle, the s_{peak} was approximately 5 to 9 times higher than for a 30° angle, whereas for the hooked series it was 1.3 to 2.3 times higher. The significant higher values of s_{peak} for a 60° angle can be ascribed to other additional mechanisms that usually occur for inclined fibres than for aligned fibres. As the fibre inclination angle increases, the stresses concentrated at the fibre bending point also increase. This leads to a more significant portion of concrete that crushes or pushes off at the crack plane. As the volume of concrete that spalls is higher, a larger fibre length is subjected to bending, resulting an additional measured slip due to the fibre deformation. So, for large inclination angles, such as 60°, the slip includes a significant parcel which is due to fibre deformation.

3.2. Uniaxial tensile tests

3.2.1. Specimens

For each batch eight cylinders with a diameter of 150 mm and 300 mm height were casted. The compressive strength of each SFRSCC batch was assessed by executing compression tests with three cylindrical specimens of 150 mm diameter and 300 mm height. At the date when the tests were performed (approximately at 30 days), the series with 30 kg/m^3 of fibres had an average compressive strength of 71.1 MPa with a coefficient of variation, CoV, of 1.9%, while in the series with 45 kg/m^3 of fibres an average compressive strength of 67.2 MPa was obtained with a CoV of 1.4%.

3.2.2. Test setup

The RILEM recommendations [17] for the execution of uniaxial tensile tests with steel fibre reinforced concrete were adopted in this work. According to this document, a notched cylinder of both 150 mm diameter and height should be used. The specimens were sawn out from standard cylinders of 150 mm diameter and 300 mm height. Afterwards, a notch along the perimeter with a 15 mm depth and 5 mm thick was swan at mid-height of the final test specimen. When the sawing operations were executed the specimens were in its hardened-mature phase. These operations were conducted with care in order to ensure that the notch become perpendicular to the specimen's axis.

Afterwards, each specimen was ground and carefully cleaned with both compressed air and solvent. The specimen was then directly glued, "in situ", to the loading platens of the testing rig. The selected glue is a high strength epoxy resin, which achieves a tensile strength of about 30 MPa and a bond strength between 4 and 8 MPa (depending on the surface material and treatment characteristics).

A servo-hydraulic system with a 2000 kN static load carrying capacity with a high stiff frame was used to perform the uniaxial tensile tests, Fig. 3a. A test was performed in closed-loop displacement control using the average signal of three displacement transducers mounted on two steel rings disposed at equal distances along the perimeter of the specimen, Fig. 3b. The adopted gauge length was 35 mm, smaller than the upper limit length of 40 mm suggested by [17]. The following displacement rates were adopted: 5 μm/min up to a displacement of 0.1 mm; 100 μm/min until the completion of the test, i.e. a 2 mm displacement.

3.2.3. Results

3.2.3.1. Stress–displacement curves. In all the performed uniaxial tensile tests, the cracking occurred along the notched plane; hence the desired crack localization was assured. The average curve and the envelope of the experimental uniaxial tensile stress–average displacement relationships, $\sigma-\delta_{avg}$, for a fibre content of 30 and 45 kg/m^3 are presented in Figs. 4 and 5, respectively. Note that δ_{avg} is the average measurement over the gauge length of 35 mm. Hereinafter these series will be designated by Cf30 and Cf45, respectively. A detailed view of the initial part of the experimental response is depicted on the right side of these figures. For both tested series the $\sigma-\delta_{avg}$ response is linear almost up to peak. Only just before the peak load some nonlinearity is observed. Once the peak load is attained, the load had a relatively accentuated decrease up to a displacement of about 0.10 mm (see right side of both Figs. 4 and 5). Beyond this displacement value, a plateau or a pseudo-hardening-plastic response has occurred. In general, the post-peak

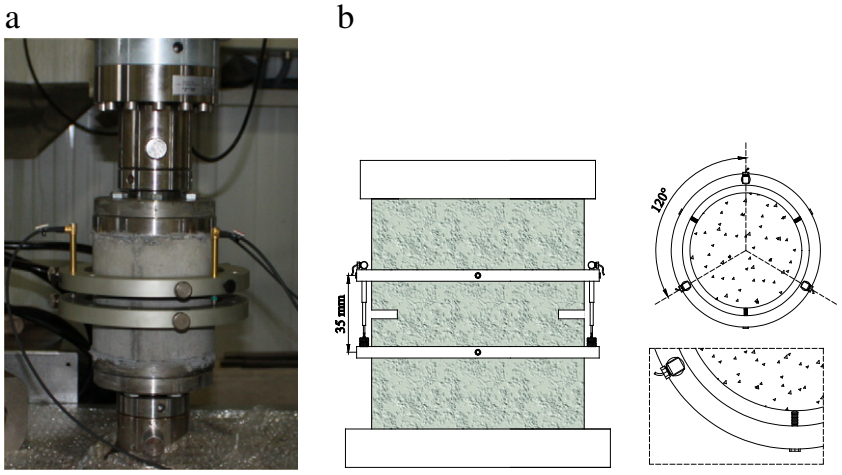

Fig. 3. Uniaxial tensile test setup: a) general view and b) positioning of displacement transducers (not scaled).

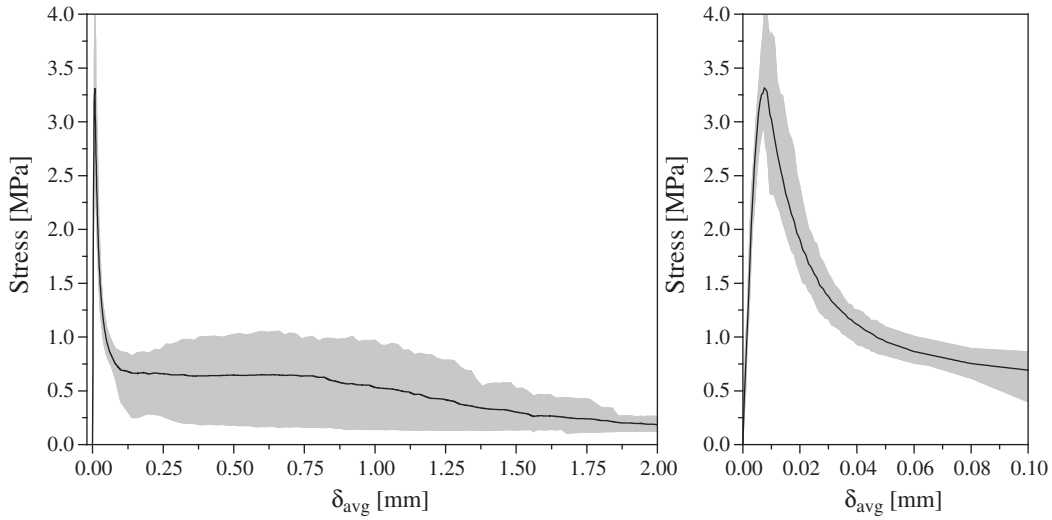

Fig. 4. Uniaxial tensile stress–displacement relationship, σ–δ_{avg}, for 30 kg/m^3.

pseudo-hardening is observed in the Cf45 series, but this response was also observed in some specimens of the Cf30 series [8]. On the other hand, after the plateau on the Cf30 series, i.e. beyond a displacement of nearby 0.8 mm, the residual stress starts to decrease with sudden strength losses corresponding to the fibre fracture. In fact, during the execution of the tensile tests this was audible by the peculiar sound of fibre fracturing.

According to Stroeven and Hu [18] the average orientation angle value of the active fibres crossing a leading crack is 35° (this value was analytically derived), and a similar value (34°) was experimentally observed by Soroushian and Lee [19]. According to the fibre pullout tests carried out, fibres at an inclination angle of 30° with the load direction lead predominantly to fibre rupture when the slip was in the range of 0.6–1.0 mm (Fig. 2b, [8]). These reasons can justify the occurrence of the significant residual stress decay after the displacement of 0.8 mm, in the result of fibres rupture in Cf30 series, where the number of active fibres is relatively reduced for the strength of the matrix.

Regarding the Cf45 series (Fig. 5), the post-peak pseudo-hardening observed can be ascribed to two reasons: a higher number of active fibres crossing the crack; both the compressive strength and stiffness of the Cf45 series matrix are lower than the Cf30, thus the fibre/matrix bond properties are not so favourable to proportionate fibre rupture. After peak load, the stress starts to decrease until a minimum stress is attained, roughly about 0.1 mm. As micromechanics of hooked ends fibre pullout demonstrate [8], above this displacement the strengthening provided by fibre's hook starts to be the predominant fibre reinforcement mechanism. Since there are more fibres intersecting the crack and due to the lower tensile strength of the concrete, the energy released during the cracking is smaller when compared to the Cf30 series. Moreover, due to the lower tensile strength and matrix stiffness, fibres did not fracture so often as in the Cf30 series. Consequently, beyond a displacement around 0.1 mm a pseudo-hardening phase occurred up to a displacement value of about 1.0 mm.

In general, the responses exhibit very low scatter in the pre-peak phase. On the other hand, in the post-peak branch the scatter was considerably higher, particularly in Cf30 series, and for a displacement higher than 0.1 mm. Up to 0.1 mm the commanding pullout reinforcement mechanism is the chemical bond [8], hence the influence of the fibre dispersion, i.e. fibre spatial distribution is not so important. As the crack width increases, the fibre's hook-ends start to be mobilized; hence the scatter of the post-peak behaviour

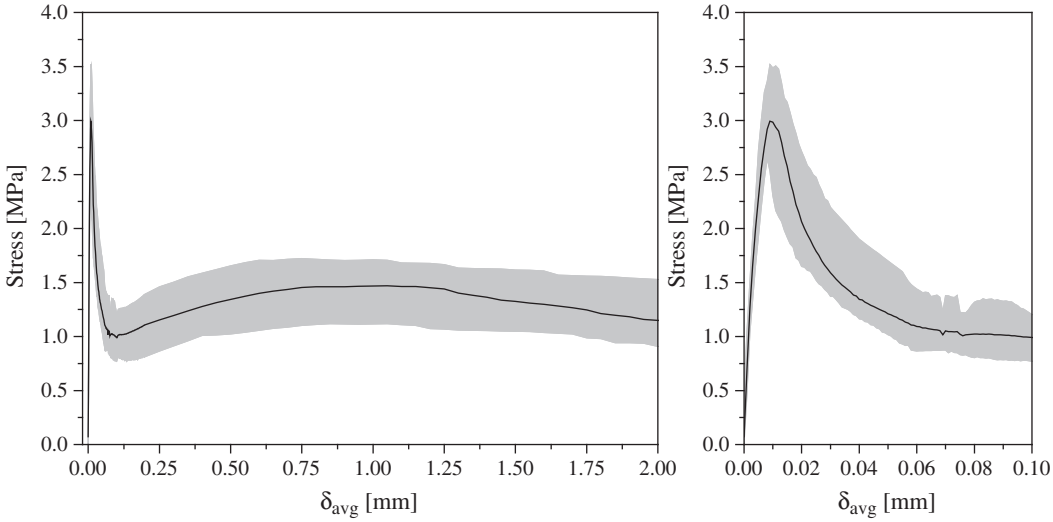

Fig. 5. Uniaxial tensile stress–displacement relationship, σ—δ_{avg}, for 45 kg/m^3.

increases due to the variation of the fibre dispersion between different specimens. Moreover, for the Cf30 series fibre rupture was the predominant fibre failure mode, as it was expected taking into account the results obtained in fibre pullout tests presented in the previous sections.

3.2.3.2. Stress–crack opening curves. In Figs. 6 and 7 are depicted the envelope of the stress–crack width curves obtained in the tests for the Cf30 and Cf45 series, respectively. A stress crack width curve ($\sigma-w$) was derived from a stress displacement curve ($\sigma-\delta$) according to the recommendations of RILEM [17]. In these figures are also included the average and the characteristic $\sigma-w$ curves. The characteristic $\sigma-w$ curve for the lower bound (L.B.) and upper bound (U.B.) with a confidence level of k = 95% was obtained from the average curve computed from all tests, $\overline{\sigma}_w(w)$, according to RILEM [17]:

$$\sigma_{w,k}(w) = \overline{\sigma}_w(w)\frac{G_{F2mm,k}}{\overline{G}_{F2mm}} \quad (1)$$

where $\overline{G}_{F2mm}$ is the average energy dissipated up to a crack width of 2 mm and $G_{F2mm,k}$ is the characteristic energy dissipated for the same crack width. For computing $G_{F2mm,k}$ a *t*-Student distribution was assumed.

3.2.3.3. Stress and toughness parameters. The average and characteristic values of relevant stress and toughness parameters, as well as the respective coefficients of variation obtained from the performed uniaxial tests are included in Table 3. In this Table σ_{peak} is the maximum stress, while $\sigma_{0.3mm}$, σ_{1mm} and σ_{2mm} are the stress at a crack width value of, respectively, 0.3, 1 and 2 mm. On the other hand G_{F1mm} and G_{F2mm} represent the dissipated energy up to a crack width of, respectively, 1 and 2 mm. The characteristic values were obtained for a k = 95% confidence level assuming a *t*-Student distribution. The number of total fibres, N_f, and effective fibres, N_f^{eff}, counted at the fracture surface are also included in Table 3. Effective fibres were considered all the fibres that had the hook deformed, as well as the fibres that have ruptured. In spite of some researchers do not consider the ruptured fibres as "effective", in the authors' opinion they should be considered, since they are able of transferring forces between the crack surfaces up to reasonable crack width. The "fully effectiveness" of this type of fibres can be questionable, but it is feasible to admit that they are "partially effective". For the sake of simplicity, let's assume that the fibre slip when it is being pulled out is approximately equal to the crack width. Then, as it can be observed in [8], in the pullout behaviour of inclined fibres, depending on the inclination angle and L_b, a fibre that fails by rupture can sustain forces up to a slip, i.e. crack width that varies from 0.7 mm to 4 mm.

From the analysis of Table 3 it is verified that, in general, the stress and toughness parameters increased with the fibre content, as it would be expected. The only exception was the peak stress which was nearby 10% lower for the series with a content of fibres of 45 kg/m^3. Note that this decrease is not due to the content of fibre, even though it could be indirectly appointed to it, since the aggregates, cement and additions contents for each series are distinct in order to attain self-compactability requirements. Moreover, the peak stress cannot be regarded as the tensile strength, but as estimation, since due to the notch introduced in specimen, apart the fact that a stress concentration exists at the notch tip, cracking does not start at the weakest material point [20].

Regarding the post-cracking stress parameters, a significant increase with the increase of fibre content was observed. A small increase of the fibre content of 15 kg/m^3 provided high increments on the values of the residual stresses, having varied from 2 to 7 times depending on the crack width value. Such increase on the residual stresses is not simply justified by the higher number of fibres crossing the crack surface for the Cf45 series. It must be noticed that there are other factors that have contributed for this fibre reinforcement effectiveness. One of these factors is the predominant fibre failure mode that, as already mentioned, was fibre rupture in the Cf30 series, while in Cf45 series was the fibre pullout.

In what concerns to the dissipated energy (G_F), in the Cf45 series a significant increase (2 to 2.6 times) up to both deflections of 1 and 2 mm was observed. In general, the CoV values obtained for the G_F parameters were considerably smaller for the Cf45 series. At a first glance, these values may seem relatively high. The magnitude of such values is, however, smaller than the ones reported by other authors with the same test procedure and specimen's dimensions for conventional fibre reinforced concrete [21,22].

In Fig. 8 is depicted the relationship between the total number of fibres, N_f, and the number of effective fibres, N_f^{eff}, at the fracture surface obtained for all the tested specimens of both Cf30 and Cf45 series. Since the uniaxial tensile test specimens (with 150 mm height) were obtained from distinct parts of a standard cylinder with 300 mm height, additionally, the specimens obtained from the bottom and upper part of the standard cylinder are distinguished in Fig. 8. This process enables an indirect assessment of an eventual influence of the

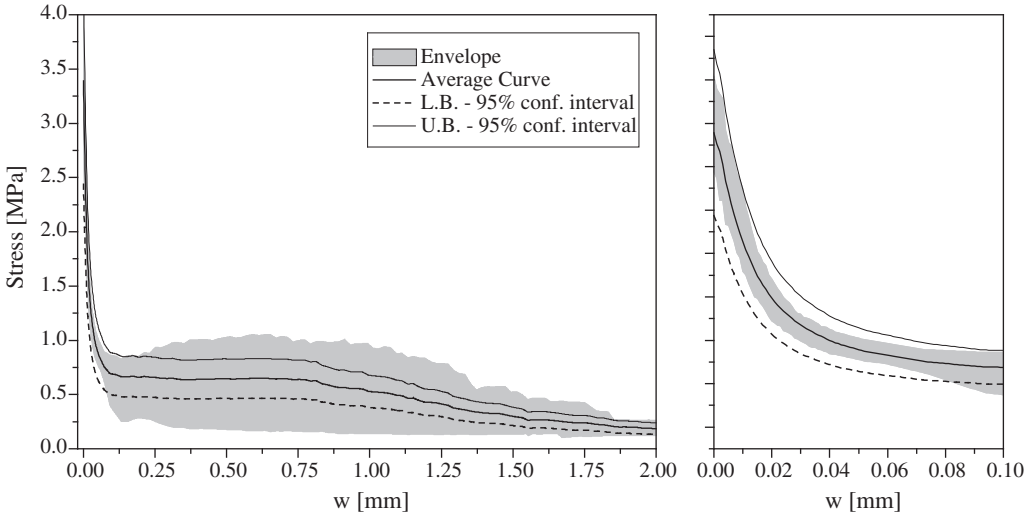

Fig. 6. Uniaxial stress–crack width relationship for 30 kg/m^3.

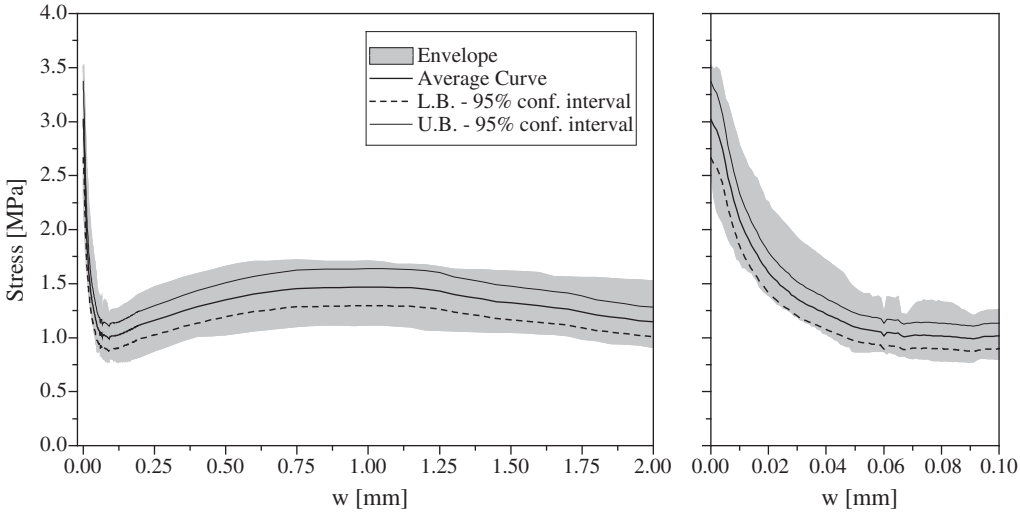

Fig. 7. Uniaxial stress–crack width relationship for 45 kg/m^3.

material specific weight (gravity) on the fibre distribution. Fig. 8 shows a linear relationship between the N_f and N_f^{eff}. Moreover, a tendency for an eventual higher concentration of fibres in the bottom part of the specimen was not found. Dupont [23] has also found a linear relationship between the total number of fibres and the number of effective fibres for small fibre contents. However, for higher fibre contents this relationship becomes nonlinear, i.e. the N_f^{eff} increment becomes smaller with the further increase of N_f. In fact, due to the group effect, N_f^{eff} may decrease as the fibre spacing decreases due to the higher probability of mutual influence of adjacent fibres [24].

3.2.3.4. Influence of the number of effective fibres on the post-cracking parameters. Throughout Fig. 9a to f are depicted the relationships between N_f^{eff} and the aforementioned post-cracking parameters obtained from the uniaxial tensile tests.

Regarding the peak stress, σ_{peak}, no significant relation was observed with the N_f^{eff} increase (Fig. 9a). In spite of σ_{peak} for the Cf45 series have been, in general, smaller than for Cf30 series, due to the reasons already pointed out, there was no significant relation between σ_{peak} and the provenience of specimen, i.e. from lower or upper part of a standard cylinder. This suggests that there was no significant segregation of the matrix skeleton and paste in the casted cylinders. On the other hand, for the residual stresses at a crack width of 0.3 mm, $\sigma_{0.3mm}$, and 1 mm, σ_{1mm}, a linear relationship between these residual stresses and the N_f^{eff} is quite evident (Fig. 9b and c). This was expected, since the residual stress sustained by the crack is intimately related to number of mobilized fibres. Concerning the Cf45 series, the residual stresses for the "top specimens" exhibited a lower scatter when compared to the values from the "bottom specimens". Due to technical problems occurred during the test program, the number of specimens from the bottom part (5) was different of the specimens obtained from the top part of the standard cylinder (3), therefore no conclusive elations can be withdraw in this subject.

The relation between the residual stress at a crack opening of 2 mm, σ_{2mm}, and the N_f^{eff} is represented in Fig. 9d. When compared to the $\sigma_{0.3mm}$–N_f^{eff} and σ_{1mm}–N_f^{eff} relationships the overall trend is distinct. First of all, there are two clear distinct trends for the σ_{2mm}–N_f^{eff} relationship. For the Cf30 series, the increase of σ_{2mm} with N_f^{eff} is marginal and can be assumed null. On the other hand, for the Cf45 series a linear increase of σ_{2mm} with N_f^{eff} is quite visible, in spite of a higher scatter than those register for the $\sigma_{0.3mm}$–N_f^{eff} and σ_{1mm}–N_f^{eff} relationships. Moreover, a clear jump on the σ_{2mm} value from the series Cf30 to Cf45 is visible, even though the small difference of N_f^{eff} between the Cf30 series' specimen with the highest N_f^{eff} and the Cf45 series with the lowest N_f^{eff}. This considerable jump on σ_{2mm} value from the Cf30 to Cf45 specimens is not ascribed to the increase of effective fibres, hence this jump comprises differences on the fibre micro-mechanical behaviour between the two series with distinct fibre content, as previously stated. Since for the series Cf30, in general, the

Table 3
Stress and toughness parameters obtained from the uniaxial tensile tests.

Cf (kg/m^3)		N_f [−]	N_f^{eff} [−]	σ_{peak} [MPa]	$\sigma_{0.3mm}$ [MPa]	σ_{1mm} [MPa]	σ_{2mm} [MPa]	G_{F1mm} [N/mm]	G_{F2mm} [N/mm]
30	Avg.	27	19	3.392	0.649	0.520	0.184	0.685	1.007
	CoV	30.8%	28.8%	13.0%	36.6%	45.1%	22.8%	32.3%	33.7%
	k95%	20	14	3.024	0.450	0.324	0.250	0.500	0.724
45	Avg.	67	39	3.019	1.219	1.466	1.342	1.342	2.645
	CoV	16.1%	16.5%	9.9%	18.0%	12.7%	13.6%	13.6%	13.1%
	k95%	58	34	2.768	1.036	1.310	1.189	1.189	2.356

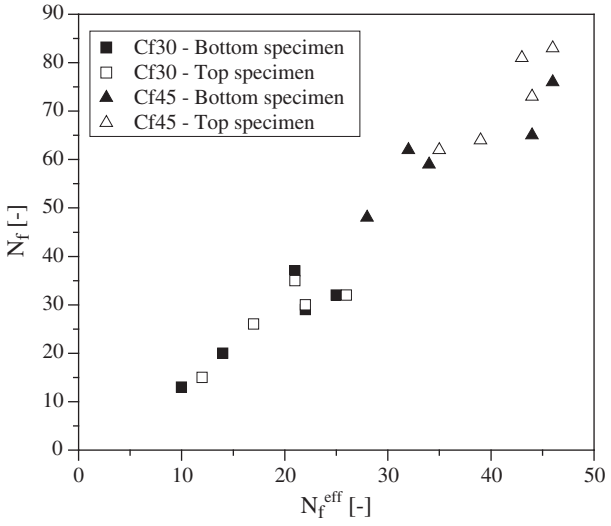

Fig. 8. Relationship between the total number of fibres and the number of effective fibres and the crack surface.

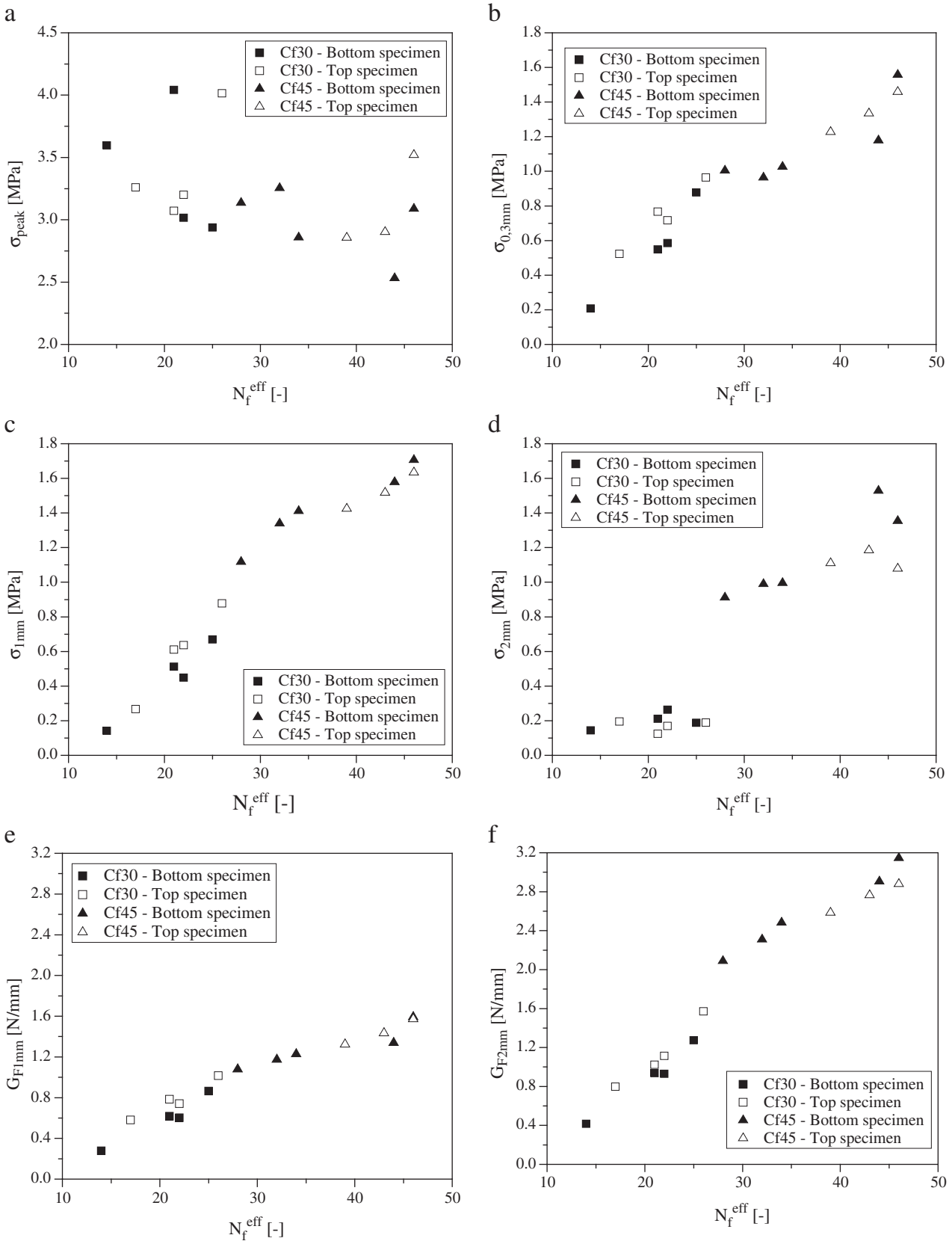

Fig. 9. Relationships between the number of effective fibres and the post-cracking parameters: (a) peak stress, (b), (c) and (d) stress at a 0.3, 1 and 2 mm crack width, respectively; (e) and (f) dissipated energy up to 1 and 2 mm crack width, respectively.

fibres ruptured before a 2 mm crack width, in case of Cf45 series, in general, the fibres were fully pulled out enabling a higher crack bridging stress transfer effectiveness.

Finally, in both series and regardless the extracting location of the specimen, the dissipated energy has shown a linear increase with N_f^{eff}, for both considered crack width limits (Fig. 9e and f). Nevertheless,

there are two aspects that should be emphasized. For the energy dissipated up to a 2 mm crack width, G_{F2mm}, there is also a jump on the G_{F2mm} value from the Cf30 to Cf45 series for the same reasons pointed for the σ_{2mm}–N_f^{eff} relationship. The other aspect is that the increment rate of both G_{F1mm} and G_{F2mm} with N_f^{eff} for the Cf45 series was slightly smaller than for Cf30 series due to the higher stiffness of the Cf30 matrix.

4. Numerical simulation

4.1. Numerical model

In steel fibre reinforced cementitious composites (SFRC), steel fibres and matrix are bonded together through a weak interface, which behaviour is important to understand the mechanical behaviour of the SFRC, since properties of the composite are greatly influenced by this interface zone [25]. Taking this into account and that the fibre contribution for the post-cracking behaviour of a composite is significantly higher than the unreinforced matrix contribution, it was settled to model the SFRC as a two phase material. In the developed model, SFRC is treated as a heterogeneous medium comprised by one homogeneous phase (aggregates and paste), and another one composed by the steel fibres. The fracture process of the cementitious matrix (unreinforced) is modelled with a multi-directional three-dimensional smeared crack model. The formulation of this crack model can be found elsewhere [26]. On the other hand, the stress transfer between crack planes due to the fibres bridging an active crack is modelled with embedded cable elements.

The random fibre distribution in the matrix is simulated with an algorithm based on the Monte Carlo method, providing a realistic distribution of the fibres in a certain specimen. In the present work only one mesh was used in the numerical simulations of the experimental tests. In [8] can be found detailed statistical information of several "virtual meshes" generated with the Monte Carlo procedure for both cylinders and prismatic specimens. The geometry, positioning and orientation of the fibres are subsequently inserted in a three-dimensional finite element mesh. This approach was adopted, mainly, due to the following reasons: 1) a homogenization of the reinforcements (fibres) crossing a certain solid element is difficult due to the random nature of the fibre distribution; 2) the discrete modelling of the reinforcements as cable elements located along the solid element nodes leads to a higher computational cost due to an unnecessary concrete mesh refinement. Moreover, this mesh refinement could lead to numerical errors caused by distorted elements for comprising the fibre distribution.

The contribution of the steel fibres crossing a solid volume is given by:

$$K^{rc} = K^{c} + \sum_{i=1}^{nf} K_i^{f} \tag{2}$$

where K^{rc}, K^{c} and K_i^{f} are, respectively, the stiffness matrix of the reinforced solid element (plain concrete + fibre reinforcement contribution), the stiffness matrix of plain concrete and the stiffness matrix of the i^{th} embedded fibre; n_f is the total number of fibres crossing the "mother" element.

A tri-linear stress–strain (σ_f–ε_f) diagram was used for modelling the fibres' bond–slip behaviour. This relationship was obtained by a manual fitting procedure of the fibre pullout tests average curves obtained for three distinct inclinations angles, α, (0°, 30° and 60°). In Fig. 10 is depicted the procedure adopted to obtain the σ_f–ε_f, where ε_f, s and L_b are, respectively, the embedded cable strain, the steel fibre's slip and the crack band-width ($L_b = 5$ mm, same as the height of the finite element where the crack is forced to appear); σ is stress computed from the pullout force, P, divided by the fibre's cross sectional area, A_f. Afterwards the completion of the σ_f–ε_f diagram's last branch, the stress transfer stops abruptly. The crack band-width is the concept implicit in the 3D smeared crack model in order to assure independence of the results from the mesh refinement [27]. The σ_f–ε_f law assigned to each embedded cable depends on the inclination angle, θ, between the cable and the normal vector of the active crack surface, $\hat{n}$ (see Fig. 11).

4.2. Simulations

The model performance is appraised by simulating the uniaxial tensile tests already presented in this work. In Fig. 12a and b are depicted, respectively, the mesh used exclusively for the concrete matrix phase and the mesh of the 3D embedded cables for the case of the self-compacting concrete reinforced with 30 kg/m^3 of steel fibres (Cf30 series). In the present mesh are used Lagrangian 8-noded solid elements for modelling the plain concrete contribution. Since the specimen had a notch at its mid-height, all the nonlinear behaviour was localized at the notch region, thus a $2\times2\times1$ Gauss–Legendre integration scheme is used (1 integration point in the loading direction). The remaining solid elements are modelled with linear elastic behaviour, and a $2\times2\times2$ Gauss–Legendre integration scheme is adopted. The Cornelissen et al. [28] softening law was used for modelling the post-cracking behaviour of SCC. The material properties of the plain concrete matrix used in the simulations are included in Table 4. These values were obtained taking into account the strength class registered for the Cf30 and Cf45 series.

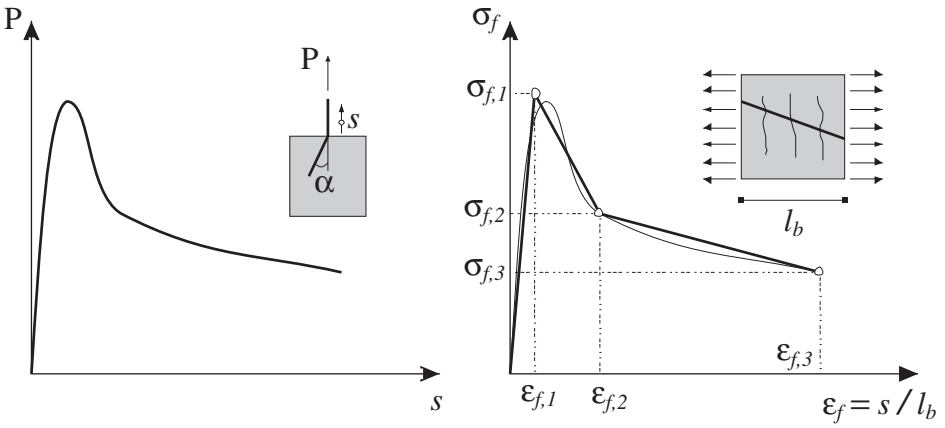

Fig. 10. Determination of the embedded cable's stress–strain diagram based on the experimental pullout force–slip relationship.

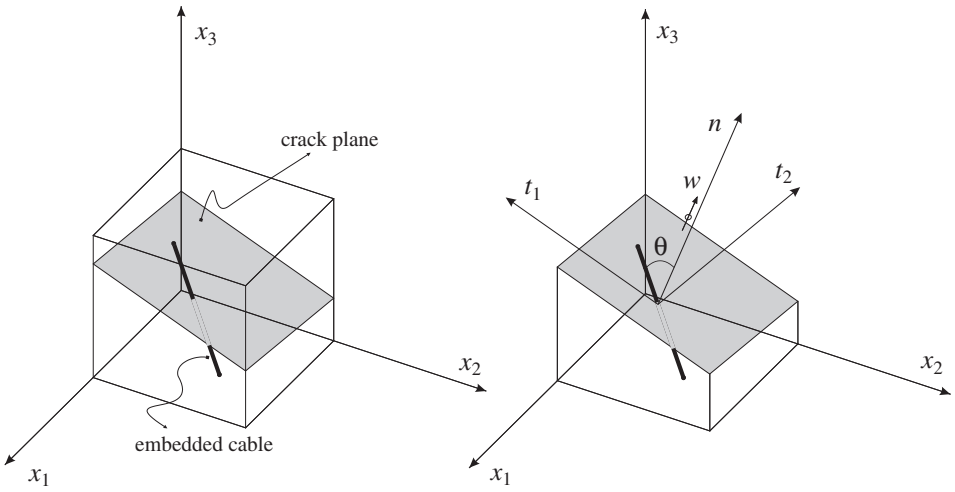

Fig. 11. Three-dimensional scheme of the embedded cable intersecting an active crack (n is the vector normal to the crack plane).

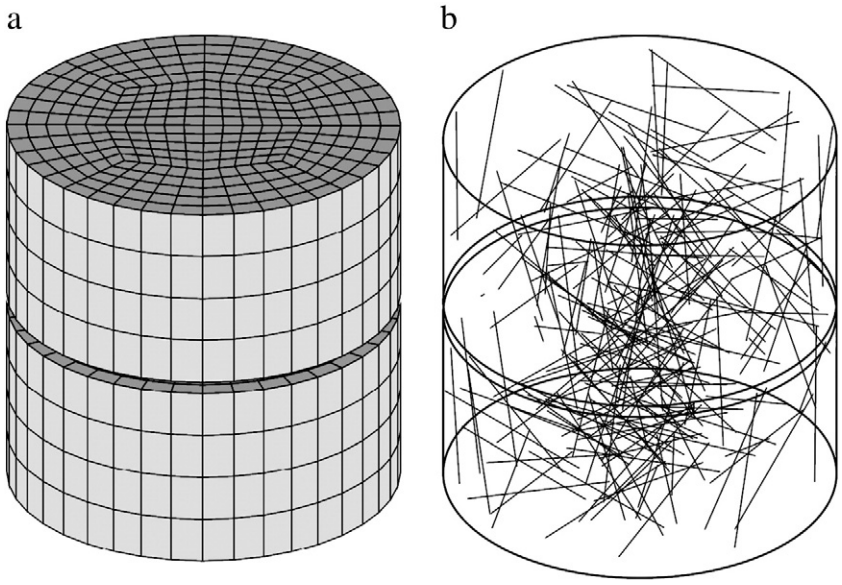

Fig. 12. Three-dimensional finite element mesh: (a) concrete phase and (b) fibre phase (Cf30 series).

On the other hand, the steel fibres are modelled with 3D embedded elements with two integration points (Gauss–Legendre). For all the embedded elements is assumed a nonlinear behaviour. From the fibre pullout tests were ascertained three distinct σ_f–ε_f laws corresponding, respectively, to the studied fibre pullout inclination angles, α (0°, 30° and 60°). Due to the impossibility of having a $\sigma-s$ law for every possible inclination angle, the $\sigma-s$ laws obtained from the pullout tests with an angle α of 0°, 30° and 60° was assigned, respectively, to the embedded cables with an orientation towards the active crack surface (θ) ranging from [0°, 15°], [15°, 45°] and [45°, 75°]. The strain in an embedded element, ε_f, is obtained from the displacement field of its "mother" element, and the corresponding slip is determined multiplying ε_f by the crack band-width. The relationships used for each α are given in Table 5.

In Figs. 13 and 14 are depicted the numerical simulation of the uniaxial tensile tests of the Cf30 and Cf45 series, respectively. Regarding the Cf30 series a good agreement with the experimental response was obtained. On the other hand, for the Cf45 series two numerical simulations were carried out. The first one adopting the $\sigma-s$ laws obtained from the fibre pullout tests (in which fibre rupture was observed for a $\alpha=30°$ and 60°). Up to a crack width of approximately 1.0 mm a relatively good agreement with the experimental response is observed. Significant stress decay is, however, observed after this crack width limit due, mainly, to the

Table 4
Plain concrete properties used in the numerical simulations.

Property	Series	
	Cf30	Cf45
Density	$\rho=2.4\times10^6$ N/mm^3	
Poisson ratio	$\nu=0.2$	
Initial Young modulus	41.3×10^3 N/mm^2	40.6×10^3 N/mm^2
Compressive strength	71.1 N/mm^2	67.2 N/mm^2
Tensile strength	4.6 N/mm^2	4.5 N/mm^2
Fracture energy	0.117 N/mm	0.114 N/mm
Crack band-width	$L_b=5$ mm (equal to the element height at the notch)	
Threshold angle	30°	

Table 5
Tri-linear stress–strain diagrams used for modelling the fibres' bond–slip behaviour.

α [°]	Failure mode	$\sigma_{f,1}$ [MPa]	$\sigma_{f,2}$ [MPa]	$\sigma_{f,3}$ [MPa]	$\varepsilon_{f,1}$ [−]	$\varepsilon_{f,2}$ [−]	$\varepsilon_{f,3}$ [−]
0	Pullout	588	803	441	0.030	0.090	0.500
30	Rupture	453	679	905	0.016	0.050	0.200
	Pullout	588	803	441	0.030	0.090	0.500
60	Rupture	283	362	656	0.020	0.160	0.400

rupture of the embedded cables with an inclination θ between 15° and 45°. Note that, the embedded cables with an inclination θ between 45° and 75° have also rupture, but only for crack widths higher than 2 mm. Since for the uniaxial tensile tests of Cf45 series, fibre rupture did not occur so often, due to both a less resistant matrix and the reduction of the average fibre orientation angle towards the crack plane, another simulation was carried out assuming that the embedded cables with an inclination θ between 15° and 45° did not rupture (see Table 5). With this approach the quality of the simulation was improved (Fig. 14).

5. Conclusions

In the present work the tensile behaviour of self-compacting concrete (SCC) reinforced with two distinct hooked end steel fibre contents (30 and 45 kg/m^3) was characterized by performing displacement controlled tensile tests. These results were discussed based upon the micro-mechanical behaviour of the steel fibres used in the composition. The fibres' micro-mechanical behaviour was assessed by means of single fibre pullout tests.

The fibre orientation (0°, 30° and 60°) and fibre embedded length (10, 20 and 30 mm) influence on the fibre pullout behaviour was studied. In general, two main pullout failures modes were observed during the pullout tests. The complete fibre pullout was observed for aligned hooked fibres, aligned smooth fibres and inclined smooth fibres, whereas for inclined hooked fibres the observed principal failure mode was fibre rupture. In general, the maximum pullout load had an almost linear increase with the L_b for both hooked and smooth fibres. Regarding the effect of the fibre orientation angle, the maximum pullout load increased up to an inclination angle of 30° and then decreased for a 60° inclination angle. For both smooth and hooked aligned fibres a slight increase of the slip at peak load with the

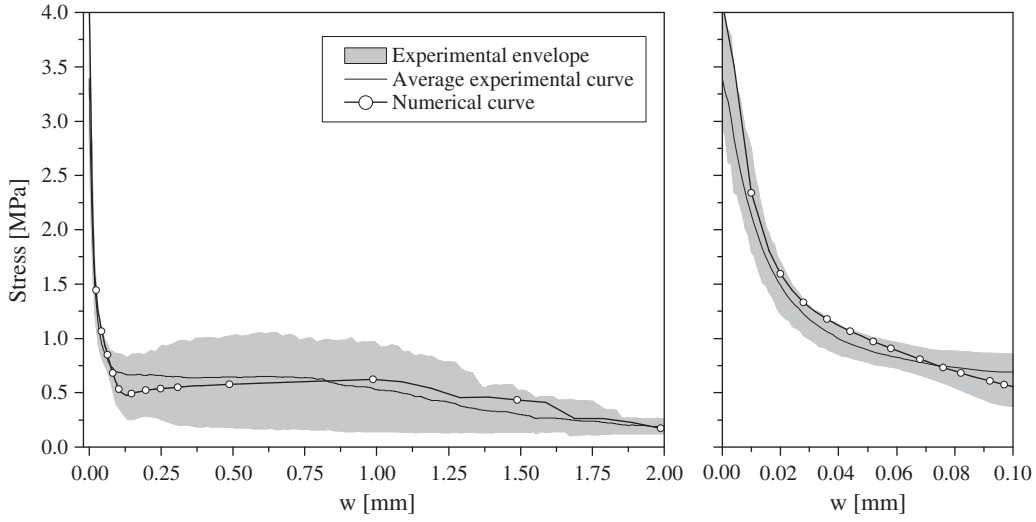

Fig. 13. Numerical simulation of the Cf30 series' uniaxial tensile tests.

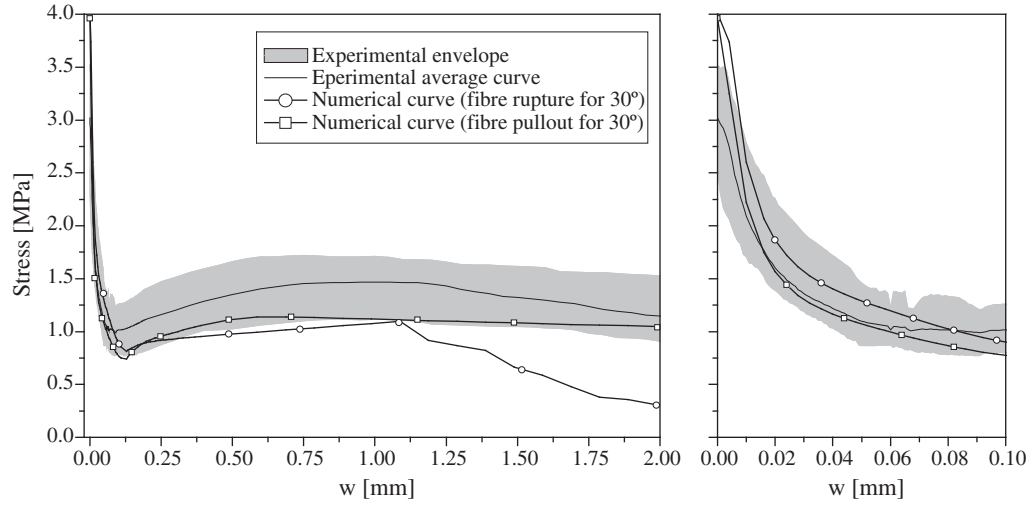

Fig. 14. Numerical simulation of the Cf45 series' uniaxial tensile tests.

fibre L_b was observed. On the other hand, regarding the influence of the fibre orientation angle, a slight increase on the slip at peak load was observed for a 30° angle, whereas for a 60° angle the slip at peak stress increased considerably. This significant increase for a 60°angle can be ascribed to other additional mechanisms that usually occur on the pullout of inclined fibres in opposite to aligned fibres. Those phenomena add to the measured slip a supplementary displacement corresponding to the fibre deformation in consequence of matrix spalling around fibre exit point.

From the stress–displacement curves obtained in the uniaxial tensile tests the stress–crack opening relationships were derived and residual stress and energy dissipation parameters, able of indicating the effectiveness of fibre reinforcement mechanisms, were determined. The relatively high compactness of the matrix system of these SFRSCC, the number of effective fibres bridging the fracture surface and the results obtained in the fibre pullout tests were all taken into account to interpret the post-cracking tensile behaviour of the tested composites. In general, a linear relationship between the post-cracking parameters and the effective number of fibres was observed. A strong dependency on the type of fibre failure mode and the stiffness of the matrix and number of effective fibres was detected, which justified the occurrence of a pseudo-hardening branch in the softening phase of the SFRSCC with the highest fibre content (Cf45 series), as well as the significant residual strength decay occurred in the SFRSCC with the lowest fibre content (Cf30). In fact, in Cf45 series the predominant failure mode was fibre pullout, while in Cf30 series fibre rupture was the predominant failure mode.

Taking the results obtained in fibre pullout tests and considering the SFRSCC as a two phase material modelled by a 3D multi-directional smeared crack model for the concrete and considering the fibres as discrete steel embedded short cables distributed in the matrix according to a Monte Carlo method, the carried out tensile test were simulated with good accuracy. With a realistic approximation of the actual fibre distribution and with the knowledge of the micro-mechanical behaviour of the fibres, it was possible to predict the macro-mechanical behaviour of laboratory's specimens.

Acknowledgements

The first author acknowledges the support provided by the grant SFRH/BD/18002/2004. The study reported in this paper forms a part of the research program PONTALUMIS, Project no. 3456, QREN. The authors also acknowledge the support of Civitest Company on the production of the SFRSCC specimens.

References

[1] K. Visalvanich, A.E. Naaman, Fracture model for fiber reinforced concrete, ACI Journal 80 (2) (1983) 128–138.
[2] V.C. Li, Y. Wang, S. Baker, A micromechanical model of tension softening and bridging toughening of short random fiber reinforced britle matrix composites, Journal of the Mechanics and Physics of Solids 39 (5) (1991) 607–625.
[3] M. Maalej, V.C. Li, T. Hashida, Effect of fiber rupture on tensile properties of short fiber composites, ASCE Journal of Engineering Mechanics 121 (8) (1995) 903–913.
[4] P. Stroeven, Stereology of concrete reinforced with short steel fibres, Fracture Mechanics and Structural Aspects of Concrete, HERON, vol. 31 (2), Delft University of Technology, Netherlands, 1986, pp. 15–28.
[5] RILEM TC 162-TDF, "Test and design methods for steel fibre reinforced concrete — design of steel fibre reinforced concrete using the σ–w method: principles and application.", Journal Materials and Structures 35 (249) (2006) 262–276.
[6] P. Stähli, R. Custer, J. Van Mier, On flow properties, fibre distribution, fibre orientation and flexural behaviour of FRC, Materials and Structures 41 (1) (2008) 189–196.
[7] L. Vandewalle, G. Heirman, F. Van Rickstal, Fibre orientation in self-compacting fibre reinforced concrete, in: R. Gettu (Ed.), Sevnth. Intnl. RILEM Symposium on Fibre Reinforced Concrete: Design and Applications RILEM Publications SARL, Chennai, India, 2008, pp. 719–728, Print-ISBN: 978-2-35158-064-6.
[8] Cunha, V.M.C.F. "Steel Fibre Reinforced Self-Compacting Concrete — from Micromechanics to Composite behaviour", PhD Thesis, University of Minho, Guimarães, Portugal, 2010.
[9] A. Van Hauwaert, J.G.M. Van Mier, Computational modelling of the fibre–matrix bond in steel fibre reinforced concrete, in: H. Mihashi, K. Rokugo (Eds.), Fracture Mechanics of Concrete Structures AEDIFICATIO Publishers, Freiburg, Germany, 1998, pp. 561–571, ISBN: 3-931681-21-1.
[10] J.P.B. Leite, V. Slowik, H. Mihashi, Computer simulation of fracture processes of concrete using mesolevel models of lattice structures, Cement and Concrete Research 34 (6) (2004) 1025–1033.
[11] J.E. Bolander, Numerical modelling of fibre reinforced cement composites: linking material scales, in: M. Prisco, R. Felicetti, G. Plizzari (Eds.), 6th RILEM Symposium on Fibre Reinforced Concretes RILEM Publications SARL, Varenna, Italy, 2004, pp. 45–60, ISBN: 2-912143-51-9.
[12] J.A.O. Barros, E.B. Pereira, S.P.F. Santos, Lightweight panels of steel fibre reinforced self-compacting concrete, Journal of Materials in Civil Engineering 19 (4) (2007) 295–304.
[13] M.D. Kotsovos, Effect of testing techniques on the post-ultimate behaviour of concrete in compression, RILEM Materials and Structures 16 (1) (1983) 3–12.
[14] EN 1992-1-1. "Eurocode 2: Design of concrete structures — Part 1: general rules and rules for buildings", European Committee for Standardization, Brussels, Belgium, 2004.
[15] A.E. Naaman, H. Najm, Bond–slip mechanisms of steel fibres in concrete, ACI Materials Journal 88 (2) (1991) 135–145.
[16] P. Robins, S. Austin, P. Jones, Pull-out behaviour of hooked steel fibres, RILEM Journal of Engineering Mechanics 35 (251) (2002) 434–442.
[17] RILEM TC 162-TDF, "Test and design methods for steel fibre reinforced concretes: Uni-axial tension test for steel fibre reinforced concrete." Journal of Materials and Structures, 34(1): 3(6), 2001.
[18] P. Stroeven, J. Hu, Effectivness near boundaries of fibre reinforcement in concrete, Materials and Structures 39 (2006) 1001–1013.
[19] P. Soroushian, C.D. Lee, Distribution and orientation of fibres in steel fibre reinforced concrete, ACI Materials Journal 87 (5) (1990) 433–439.
[20] J.G.M. Van Mier, M.R.A. Van Vliet, Uniaxial tension test for the determination of fracture parameters: state of the art, Journal of Engineering Fracture Mechanics 69 (2002) 235–247.
[21] Barragan, B. E. "Failure and Toughness of Steel Fibre Reinforced Concrete under Tension and Shear". Ph.D. thesis, Universitat Politecnica de Catalunya, Barcelona, Spain, 2002.
[22] I. Läofgren, H. Stang, J.F. Olesen, The WST method, a fracture mechanics test method for FRC, Materials and Structures 41 (2008) 197–211.
[23] Dupont, D. "Modeling and experimental validation of the constitutive law (σ–ε) and cracking behaviour of steel fibre reinforced concrete". PhD Thesis, Department of Civil Engineering, Catholic University of Leuven, Belgium, 2003.
[24] A. Naaman, S. Shah, Pullout mechanism in steel fibre reinforced concrete, ASCE Journal of the Structural Division, 102 (8) (1976) 1537–1548.
[25] Pereira, E.N.B., "Steel Fibre Reinforced Self-compacting Concrete: from material to mechanical behaviour", dissertation for Pedagogical and Scientific Aptitude Proofs, Department Civil Engineering, University of Minho, 188pp, <http://www.civil.uminho.pt/composites>2006.
[26] Z.P. Bazant, B.H. Oh, "Crack band theory for fracture of concrete", materials and structures, RILEM 16 (93) (1983) 155–177.
[27] H.A.W. Cornelissen, D.A. Hordijk, H.W. Reinhardt, Experimental determination of crack softening characteristics of normal weight and lightweight concrete, Heron, Fracture Mechanics and Structural Aspects of Concrete 31 (Nº 2) (1986) 45–56.
[28] A. Ventura-Gouveia, J.A.O. Barros, A.F.M. Azevedo, J.M. Sena-Cruz, Multi-fixed smeared 3D crack model to simulate the behaviour of fibre reinforced concrete structures, CCC 2008 — Challenges for Civil Construction, Paper T2–3, 2008, 11pp., FEUP, Porto.